# Redshift of Earthquakes via Focused Blind Deconvolution of Teleseisms

**Pawan Bharadwaj[1,2], Chunfang Meng[2], Aimé Fournier[2], Laurent Demanet[1,2], Mike Fehler[2]**

[1]Department of Mathematics, Massachusetts Institute of Technology
[2]Earth Resources Laboratory, Massachusetts Institute of Technology

**Key Points:**

- We present a data-driven factorization method of surface teleseisms into source and path-related signals.
- The method outputs the earthquake source spectrum and its variation with azimuth to implicate rupture propagation.
- The method allows us to estimate the rupture modes even in the absence of near-source stations.

## Abstract

We present a robust factorization of the teleseismic waveforms resulting from an earthquake source into signals that originate from the source and signals that characterize the path effects. The extracted source signals represent the earthquake spectrum, and its variation with azimuth. Unlike most prior work on source extraction, our method is data-driven, and it does not depend on any path-related assumptions e.g., the empirical Green's function. Instead, our formulation involves focused blind deconvolution (FBD), which associates the source characteristics with the *similarity* among a multitude of recorded signals. We also introduce a new spectral attribute, to be called redshift, which is based on the Fraunhofer approximation. Redshift describes source-spectrum variation, where a decrease in frequency occurs at the receiver in the opposite direction of unilateral rupture propagation. Using the redshift, we identified unilateral ruptures during two recent strike-slip earthquakes. The FBD analysis of an earthquake, which originated in the eastern California shear zone, is consistent with observations from local seismological or geodetic instrumentation.

## Plain Language Summary

The hazard assessment of large earthquakes is closely related to the propagation of their associated ruptures. This research responds to numerous fundamental challenges involved in directly measuring source signals that originate from a propagating rupture. It is desirable to directly measure the source pulses at the seismometers and subsequently infer quantities that are related to the rupture propagation. However, the signals measured in place of those pulses are affected by the subsurface properties through which they propagate before reaching these stations. Thus, instead of measuring the earthquake source signal directly, each seismic station records two types of information that are convolved into a single signal: information about the earthquake (source pulse) and information about the unknown subsurface features through which waves passed (path effects). Consequently, an accurate characterization of an

Corresponding author: Pawan Bharadwaj, pawbz@mit.edu

earthquake rupture involves reliably analyzing the recorded seismograms to separate the path effects from the source pulses. Current methods for separating out the two types of information rely on unreliable assumptions, and may be confounded because extracting source pulse requires assumptions about the path, but conversely extracting path effects requires assumptions about the source. In this paper, we introduce to seismology a new analysis method, "focused blind deconvolution", that can be used to extract source or path information without relying on traditional assumptions. Instead, this method compares data from the same source picked up by multiple receivers, and uses advanced signal processing to identify similarities and differences among the data. Similarities among the signals can be identified as source effects, while dissimilarities indicate path effects. Because it does not require the aforementioned assumptions, this method will provide more accurate and reliable information to seismologists.

## 1 Introduction

Identifying the dominant rupture characteristics of earthquakes is important for evaluating the earthquake hazard (Heaton & Helmberger, 1977; Olson & Apsel, 1982; Somala et al., 2018; Gallovic et al., 2019). In order to do so, we consider source extraction (Ulrych, 1971; Clayton & Wiggins, 1976) mainly from the first arriving surfaces waves, termed as R1 (Rayleigh) and G1 (Love) waves, contained in the long-period records of intermediate-magnitude strike-slip earthquakes. The primary difficulty associated with this extraction is: instead of measuring the earthquake source signal, each seismic station records a spatio-temporal convolution between the source $s$ and the complex subsurface Green's function $g$ that is unknown. As $g$ depends on the unknown subsurface characteristics e.g., its structure and intrinsic attenuation, an accurate characterization of the earthquake involves a *blind factorization* of the ground motion data into two terms that represent the source and path effects separately. To our knowledge, this paper presents the first demonstration of the required factorization, thanks to a recent advance in deconvolution methodology, namely "focused blind deconvolution" (FBD, introduced by Bharadwaj et al., 2019). Our factorization provides complementary information on the rupture characteristics compared to existing methods that rely on isolating (e.g, Tocheport et al., 2007) the P-wave arrivals for back-propagation (Larmat et al., 2006; L. Meng et al., 2016; Yin & Denolle, 2019) and/or construction of an empirical Green's function (EGF, Hartzell, 1978; Lanza et al., 1999; McGuire, 2004; Vallée et al., 2011; Vallée & Douet, 2016; Kikuchi & Kanamori, 1982; Lay et al., 2009).

The factorization of the seismograms is challenging and generally not solvable, because of the unknown trade-off between $s$ and $g$ i.e., extracting one requires assumptions about the other. However, FBD compares a multitude of records (e.g., Plourde & Bostock, 2017) due to the same source, and identifies the *similarities* among them through a formal analysis. Subsequently, it associates the similarities to the spectrum of $s$, and the dissimilarities to $g$. For the success of FBD, we require that the receivers span a wide range of azimuth-angles and distances with respect to the rupture. In recent years, large numbers of seismometers have been deployed, so this requirement can easily be satisfied.

## 2 Redshift in an Earthquake Spectrum

Our primary goal is the robust estimation of the earthquake source spectrum using the aforementioned factorization of the teleseismic waveforms. In this section, we first assume a kinematic source model for a fault that is vertical. Then, we associate the parameters of this source model to the features e.g., redshift or Doppler shift in the estimated source spectrum.

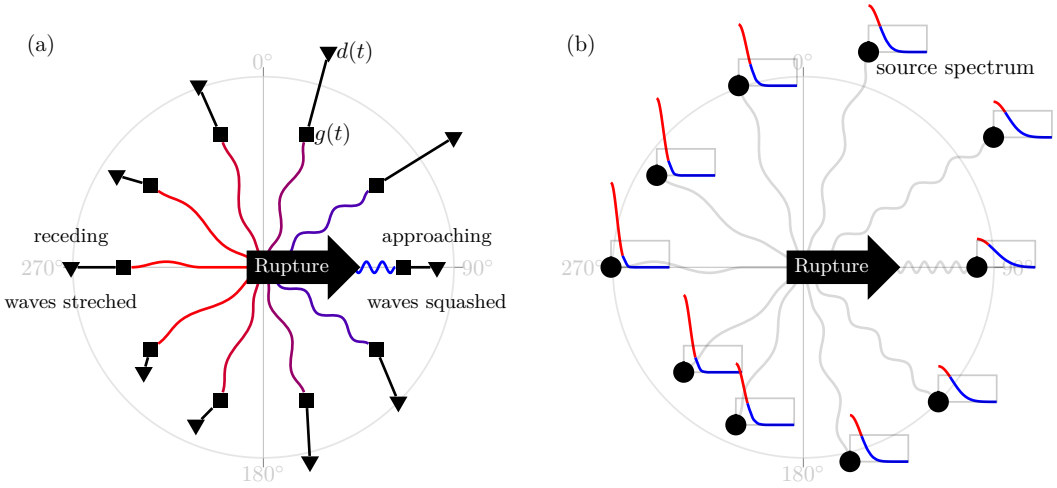


**Figure 1.** Schematic of waves emitted due to a rupture propagating from west (azimuth $\theta = 270°$) to east (90°). a) Blue waves emitted towards the east are shortened, while the red waves traveling towards the west are lengthened. These waves undergo complex scattering (squares) before they reach the receivers (triangles), resulting in a challenging source-spectrum estimation problem. b) FBD factorizes the measurements for effectively removing the squares and directly estimating the source spectra (red-blue graphs) at the (circles) receivers. The variability of the normalized source spectrum with $\theta$ can be used to infer the kinematic rupture parameters.

We set a cylindrical coordinate system with origin $O$, radius $r$, azimuth $\theta$, and height $z$. The fault plane extends from $r = 0$ to $L$ along the radial line $\theta = 90°$, and from $z = 0$ to $H \ll L$ along the cylindrical axis. A unidirectional rupture starts at the hypocenter, located at $O$, and propagates along the radial line. The kinematic rupture model, explained in Appendix A, is simplified using the Fraunhofer approximation to represents the waves recorded at $(r, \theta)$ on the surface $z = 0$ as:

$$d(t; r, \theta) \approx s(t; \theta) *_t g(t; r, \theta). \tag{1}$$

Here, the path effects are denoted by a convolution operation (eq. A7) in time with a function $g(t; r, \theta)$, which corresponds to the response due to impulsive force couples acting at the hypocenter. The apparent source pulse emitted in the direction of azimuth $\theta$ is given by the function:

$$s(t; \theta) = \begin{cases} \frac{c_r}{|\gamma|} w\left(\frac{t c_r}{\gamma}\right) & \text{when} \quad 0 < \frac{t c_r}{\gamma} < L; \\ 0 \quad \text{otherwise,} \end{cases} \qquad \text{where} \quad \gamma = 1 - \frac{c_r}{c} \sin\theta. \tag{2}$$

In the above equation, $\gamma$ roughly varies between 0 and 2, owing to the common observation that rupture speed $c_r$ is comparable to wave velocity $c$. The function $w$ depends on $H$ and represents the distribution of stress drop along the radial line of the fault. (Note that we have substituted $\psi = \theta - 90°$ in eq. A5 — this substitution is only valid for the waves that depart from the fault along radial lines — so in section 4.3, we primarily analyze the surface waves emitted from steeply-dipping faults.)

The source model in eq. 2 is less restrictive compared to a model that regards the fault as a stationary point source i.e., it also incorporates the seismic wavelength $\lambda$ that is comparable to $L$. However, as in eq. A4, it requires that the receivers are located at large distances such that $r \gg 2L^2/\lambda$. Accordingly, in section 4.3, we analyze the above-mentioned surface waves in the long-period seismograms:

- recorded at teleseismic distances with $r > 1600\,\text{km}$ i.e., epicentral distance greater than 15°;
- that contain dominant frequencies less than $0.1\,\text{Hz}$ — as a result $\lambda \gtrsim 40\,\text{km}$;
- from intermediate-magnitude ($6.0 < \text{Mw} < 6.5$) earthquakes typically with $L \approx 60\,\text{km}$.

In eq. 2, it can be noted that the source function $w$ is scaled depending on

1. the speed $c_\text{r}$ of the rupture propagation;
2. the direction $\theta$ relative to the rupture propagation;
3. and the velocity $c$ of the propagating waves in the source region.

Therefore, if the rupture is approaching ($\theta = 90° \Rightarrow |\gamma| \ll 1$) a station then the source function $w$ is shortened as depicted in Fig. 1a. Accordingly, as a result of the scaling property of the Fourier transform, its amplitude spectrum is lengthened over the frequency $\omega$, as shown in the Fig. 1b. On the other hand, if the rupture is receding ($\theta = 270° \Rightarrow \gamma = 1 + c_\text{r}/c \approx 2$) from a station then the source function $w$ is lengthened in time, resulting in a shortened-frequency amplitude spectrum of the source. This causes an apparent shift in the corner frequency, which is considered in the Haskell fault model (Madariaga, 2015).

Unfortunately, the time-scaled source pulse i.e., the apparent source pulse $s$ is affected by the properties of the subsurface that the signal propagates through before reaching these stations. Such effects prevent us from directly observing the apparent source pulse at the stations. In the following sections, we will present a factorization of the records $d$ of an earthquake to eliminate the path effects, as depicted in Fig. 1.

## 3 Focused Blind Deconvolution

FBD requires that the multiple receivers span a wide range of azimuth-angles $\theta$ and distances $r$ relative to the rupture. For such a set of receivers, a temporal-index window $t \in \{T_1, \ldots, T_2\}$, relative to the origin time of the earthquake, has to be applied in order to roughly isolate either the body waves or the surface waves. Depending upon the temporal window, FBD outputs an estimate $|\hat{S}|$ of the source spectrum $|S|$ (of either P- or S-waves) as a function of $\theta$. We consider many azimuthal bins $\Theta$, each with $n$ receivers, such that the variability of each $|\hat{S}|\Big|_{\theta\in\Theta}$ can be ignored. Therefore, we have $s(t;\theta) \approx s(t)\ \forall\theta \in \Theta$, resulting in a single-input multiple-output model

$$d_i(t) = s *_t g_i. \tag{3}$$

Here, the subscript $i \in \{1, 2, \ldots, n\}$ denotes an index of a receiver that records the ground motion $d_i(t)$, or else a spatial location where the Green's function $g(\cdot, t)$ is evaluated as $g_i(t)$. We denote a vector of records by $[d_i] : \{T_1, \ldots, T_2\} \to \mathbb{R}^n$, and a vector of Green's functions by $[g_i] : \{T_1, \ldots, T_2\} \to \mathbb{R}^n$. The duration length of each element of $[d_i]$ and $[g_i]$ is given by $T_2 - T_1 + 1$, which was chosen so that the $d_i$ may each contain an identical source pulse $s : \{0, \ldots, T\} \to \mathbb{R}$. It is important to note that the FBD results are insensitive to the choice of the duration length $T + 1$ of $s$ — as long as the length is long enough to capture the source effects.

In every $\Theta$, the intention is to factorize (i.e., blindly deconvolve) the ground motion $[d_i]$ in eq. 3 into the path effects $[g_i]$ and the source $s$, with *much fewer and simpler assumptions* about these factors, compared to those made in conventional methods. A suitable algorithmic approach, related to multichannel blind deconvolution (BD), is a least-squares fit of $[d_i]$ to jointly optimize two unknown functions $[g_i]$ and $s$. The joint optimization can be suitably carried out using alternating minimization (Ayers & Dainty, 1988; Sroubek & Milanfar, 2012): in one cycle, we fix one function

and optimize the other, and then fix the other and optimize the first. Several cycles are expected to be performed to reach convergence. However, it is well known that BD is not solvable, due to non-uniqueness, without making assumptions on at least one of the two unknowns. These assumptions determine the admissible trade-off between $[g_i]$ and $s$ during the optimization.

Accordingly, we employ focused blind deconvolution (FBD), which first reduces the trade-off in BD by considering a least-squares fitting of *interferometric* or *cross-correlated* records, instead of the raw records. And second, it determines all the remaining trade-off (except for a scalar) by associating the *dissimilarities* among the multiple records to $[g_i]$, while attributing similarities to $s$. Our examples below demonstrate that these associations are valid as long as the receivers are placed at dissimilar locations i.e., their separation distances are much larger than the wavelength.

FBD is presented in detail by Bharadwaj et al. (2019), we discuss the underlying principles below. An illustrative numerical experiment, along with an open-source software package, is presented in the supplementary material. One import aspect of FBD is the following reformulation that is simpler to solve, due to the reduced trade-off, as it only estimates the unknown source auto-correlation and interferometric path effects.

**Definition 1** (IBD: Interferometric Blind Deconvolution)**.** The interferometric record between $i$th and $j$th receivers is given by

$$d_{ij}(t) = \{d_i \otimes d_j\}(t) = \{\underbrace{s \otimes s}_{s_\mathrm{a}}\} *_t \{\underbrace{g_i \otimes g_j}_{g_{ij}}\},$$

where $\{u \otimes v\}(t) = u(-\cdot) *_t v$ defines temporal cross-correlation. IBD aims for a least-squares fitting of an $(n+1)n/2$-vector, denoted by $[d_{11}, d_{12}, \ldots, d_{22}, d_{23}, \ldots, d_{nn}]$ or simply $[d_{ij}]$, of the unique interferometric records between every possible receiver pair:

$$(\hat{s}_\mathrm{a}, [\hat{g}_{ij}]) = \underset{s_\mathrm{a}, [g_{ij}]}{\arg\min} \sum_{k=1}^{n} \sum_{l=k}^{n} \sum_{t=-T_2+T_1}^{T_2-T_1} \{d_{kl}(t) - \{s_\mathrm{a} * g_{kl}\}(t)\}^2. \tag{4}$$

Along the similar lines of BD, it jointly optimizes two functions, namely the interferometric Green's function $[g_{ij}]{:}\{-T_2{+}T_1, \ldots, T_2{-}T_1\} \to \mathbb{R}^{(n+1)n/2}$ and the auto-correlated source function $s_\mathrm{a} : \{-T, \ldots, T\} \to \mathbb{R}$.

The motivation behind dealing with $[d_{ij}]$ is that the cross-correlation operation discards the phase information from the Fourier representation of the source. Therefore, the admissible trade-off between the path effects $[g_{ij}]$ and the source $s_\mathrm{a}$ is reduced, compared to trade-off between $[g_i]$ and $s$ in BD. The remaining trade-off, pertaining to the amplitude spectrum of the source, is determined in FBD by regularizing with a focusing functional:

$$J = \sum_{k=1}^{n} \sum_{t=-T_2+T_1}^{T_2-T_1} t^2 g_{kk}(t)^2.$$

FBD minimizes $J$ i.e., the energy of the auto-correlated Green's functions $g_{ii}$ multiplied by the lag time to result in a solution where the $g_i$ are heuristically as white (in the frequency domain) as possible. As shown by Bharadwaj et al. (2019), simultaneously maximizing the whiteness of any $g_i$ promotes its dissimilarity from all the $g_{j\neq i}$. Therefore, for the success of FBD, it is important that the true $g_i$ are sufficiently dissimilar. For instance, in the limit that the true $g_i$ are equal to each other, FBD just outputs the temporal Kronecker $\delta(t)$ for the $g_i$, making the $s$ equal the $d_i$. In our experiments, we ensure that the "sufficiently dissimilar" requirement is satisfied by choosing receivers separated by distance $r$ much larger than the wavelength. Note

that, for a given receiver configuration, the width $|\Theta|$ of each azimuthal bin $\Theta$ determines the range of $r$; we choose each $|\Theta|$ sufficiently large such that receivers span a wide range of $r$.

Now, after estimating source auto-correlation in every $\Theta$, the next step is to normalize them such that $\hat{s}_{\mathrm{a}}(0) = 1$. Then, the Fourier representation of $\hat{s}_{\mathrm{a}}$ can be used to construct the normalized source spectrum. For every $\Theta$, the duration of the apparent source time function is given by the time necessary for the envelope of $\hat{s}_{\mathrm{a}}$, denoted by $E(\hat{s}_{\mathrm{a}})$, to decrease below a chosen threshold. The envelope operator $E$ computes the absolute value of the analytic representation of a real-valued signal. The final trivial step is to combine the outputs together over all $\Theta$ to form the estimated source properties over the entire interval of $\theta$.

## 4 Applications

For a given earthquake, FBD estimates the apparent source auto-correlation $\hat{s}_{\mathrm{a}}(t;\theta)$, and its zero-phase Fourier representation i.e., the apparent power spectrum $|\hat{S}(\omega;\theta)|^2$. The benefits of this methodology include:

1. at any given azimuth $\theta$, the time duration of the apparent source pulse can be determined using that of $\hat{s}_{\mathrm{a}}$;
2. $|\hat{S}(\omega;\theta)|$ can be inspected for spectral attributes associated with source characteristics e.g., its closeness to a unilateral rupture;
3. more generally, $|\hat{S}(\omega;\theta)|$ can be used as input to finite-fault inversion to directly infer the rupture parameters, without being affected by the uncertainties in the subsurface models;
4. assuming that multiple earthquakes share identical path effects, the variation of $|\hat{S}(\omega;\theta)|$ among these earthquakes provides an accurate relative magnitude of each earthquake.

Now, we demonstrate the first two benefits, while leaving the others for future research.

### 4.1 Redshift Attribute

Redshift is a spectral attribute of an almost unilaterally propagating rupture. It is related to the frequency-scaling of the source spectrum as discussed in section 2. For a given earthquake spectrum and a choice of two different frequency bands, red and blue for low- and high-frequency bands respectively, we:

1. compute the spectral energy of $|\hat{S}|$ in the bands as a function of the azimuth $\theta$, resulting in a spectral-energy vs azimuth plot;
2. and inspect if the energy in the red band is dominant in a particular direction, corresponding to a dominant blue energy in the opposite direction; this characteristic of the source-spectrum variation is referred to as redshift.

Inspecting the FBD estimated (normalized) source spectra $|\hat{S}(\omega;\theta)|$ for redshift will help us identify unilateral ruptures from those that are more complex. The redshift attribute is quantifiable using the wide-band ambiguity function (Weiss, 1994; Sibul & Ziomek, 1981), which we also leave for future research.

### 4.2 Synthetic Experiment

We now present a 2-D numerical experiment that demonstrates the benefits of FBD for rupture characterization. We record both the horizontal- and vertical-component displacement due to a unilaterally propagating rupture along $\theta = 90°$. As

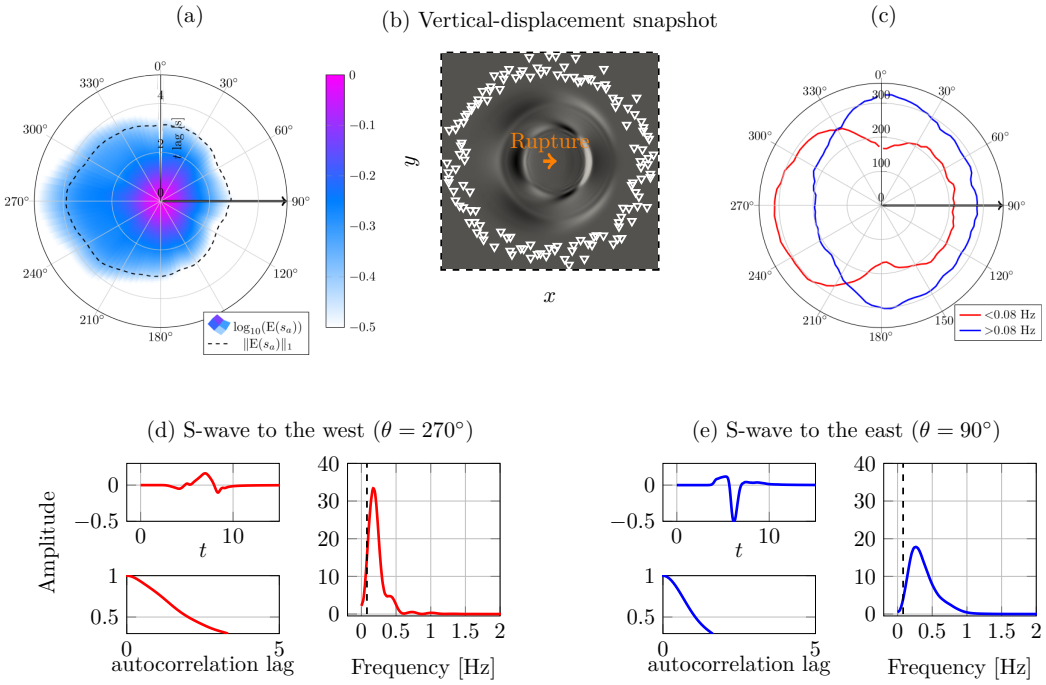


**Figure 2.** A synthetic experiment. a) The envelope of the FBD-estimated auto-correlated source pulse i.e., $E(\hat{s}_a(t;\theta))$ is plotted as a function of the lag time and azimuth. b) Vertical displacement due to a rupture, colored in gray-scale as a function of the horizontal $x$ and vertical $y$ spatial coordinates, before the P and S waves are scattered by the boundaries (dashed lines) of the medium. Some of the receiver positions are marked by white triangles. c) The energy of the FBD-estimated source spectrum, in both the low (red) and high (blue) frequency bands, is plotted to depict the redshift. In order to validate the FBD results, the direct S-wave pulse on the opposite sides of the rupture is plotted in (d) and (e), respectively. The dashed vertical line separates the two frequency bands of (c).

depicted in Fig. 2b, roughly 100 receivers surround the source and span a range of distances $r$ from 15 to 32 km. The waves are modeled using an elastic finite-element solver (C. Meng & Wang, 2018) in a homogeneous spatial domain with both $x$ and $y$ from $-32$ to 32 km. We deliberately set reflective, instead of absorbing, boundary conditions to create complex path-specific effects due to multiple scattering. This 2-D experiment only involves the scattered P and S waves, but similar experiments can also be performed using surface waves, which are considered later.

We employ FBD to estimate $\hat{s}_a(t;\theta)$ from the full-wavefield records — the envelope of $\hat{s}_a$ is plotted in Fig. 2a with lag time $t > 0$ on the radial axis and $\theta$ on the azimuthal axis. We isolated the S-wave pulses from the records at 90° and 270°, respectively, and plotted them in Figs. 2d and 2e. Observe that the difference in their durations, as depicted by the envelopes of the auto-correlated pulses, is consistent with our FBD result. Similarly, we plotted the normalized spectra of the S-wave pulses in these plots to observe that the pulse at 270° has dominant low frequencies compared to that at 90°. Again, this is consistent with FBD-estimated spectral energy vs azimuth plot in Fig. 2c.

### 4.3 Application to Recorded Earthquakes

We now use FBD in the source-spectrum analysis of two earthquakes with magnitude Mw $\leq$ 6.5. In recent years, a large number of seismometers have been deployed, which facilitate the capture of the source pulse at a wide range of azimuths $\theta$ and distances $r$, making FBD application feasible. With regard to the source model discussed in the previous sections, we only consider strike-slip earthquakes that ruptured almost-vertical faults at shallow depths of $\approx$ 15 km. The earthquake locations and moment-tensor solutions (Dziewonski et al., 1981; Hanka & Kind, 1994) are plotted in the Fig. 3. Additional information about these earthquakes is provided in the supplementary material. For each earthquake, we have downloaded long-period records, with 1 Hz sampling rate, from 20 supported international data centers that can be accessed via the toolbox obspyDMT (Hosseini & Sigloch, 2017). Only stations with epicentral distance greater than 15° were selected, as plotted in the Figs. 3a and 3d. At each seismic station, we utilize multiple components of the recorded displacement, which primarily contain the first-arriving surfaces waves, termed as R1 (Rayleigh) and G1 (Love) waves, that are the largest-amplitude arrivals.

The pre-processing of the records is relatively simple, performed using the toolbox ObsPY (Beyreuther et al., 2010). We first remove the noisy records, and demean the records we keep. We then perform an important step i.e., instrument correction, without which we notice that the instrument response contaminates the FBD-extracted similarity among the records. Again, note that we associate the similarity among the records with the source effects; therefore, it is important that there is no *artificial* similarity in the recorded spectra due the instrument response of the seismometers. Finally, the records were windowed for a duration $\approx$ 6750 s following the origin time, resulting in $d(t; r, \theta)$ as input to FBD.

#### *4.3.1 Nicobar (08 November 2015)* Mw=6.5

This strike-slip earthquake ruptured a known fault in a region SE of the Andaman Island (see supplementary material). The teleseismic stations that were utilized in the FBD analysis are plotted in Fig. 3a. The estimated apparent source pulse auto-correlation $\hat{s}_{\mathrm{a}}$, plotted in Fig. 3b, indicates that the source duration is $\approx$ 15 s longer in the NW compared to the SE direction. In the spectral energy vs azimuth plot, the spectral energy is computed in three different frequency bands as plotted in Fig. 3c. These results, similar to those in Figs. 2b and 2c, indicate a unilateral rupture propagation, along the SE trend. Accordingly in Fig. 4, the source spectrum exhibits frequency scaling, with higher corner frequency in the direction of the rupture propagation, and vice versa. The rupture propagation is consistent with one of the two possible strike directions indicated by the moment tensor in the Fig. 3a.

#### *4.3.2 California (04 July 2019)* Mw=6.4

This is a foreshock of the Mw = 7.1 July 5 mainshock in the 2019 Ridgecrest sequence that occurred as the result of shallow strike slip faulting in the crust of the North America plate. The FBD analysis of the July 5 mainshock (USGS, 2019b) is presented in the supplementary material. Compared to the mainshock, the FBD-extracted spectrum for this earthquake indicates a relatively simple rupturing, with dominant propagation towards SW. That is: 1) a shorter source duration is noticed in the SW direction relative to NE, as shown by the $\hat{s}_{\mathrm{a}}$ plot in Fig. 3e; 2) the stations in the SE direction record dominant high frequencies — as is evident from the spectral-energy vs azimuth plot in Fig. 3f. These results are consistent with the direct observations, which suggest that the event ruptured a previously unnoticed NE-SW trending fault. Moreover, the aftershocks following this particular event also aligned along the NE-SW

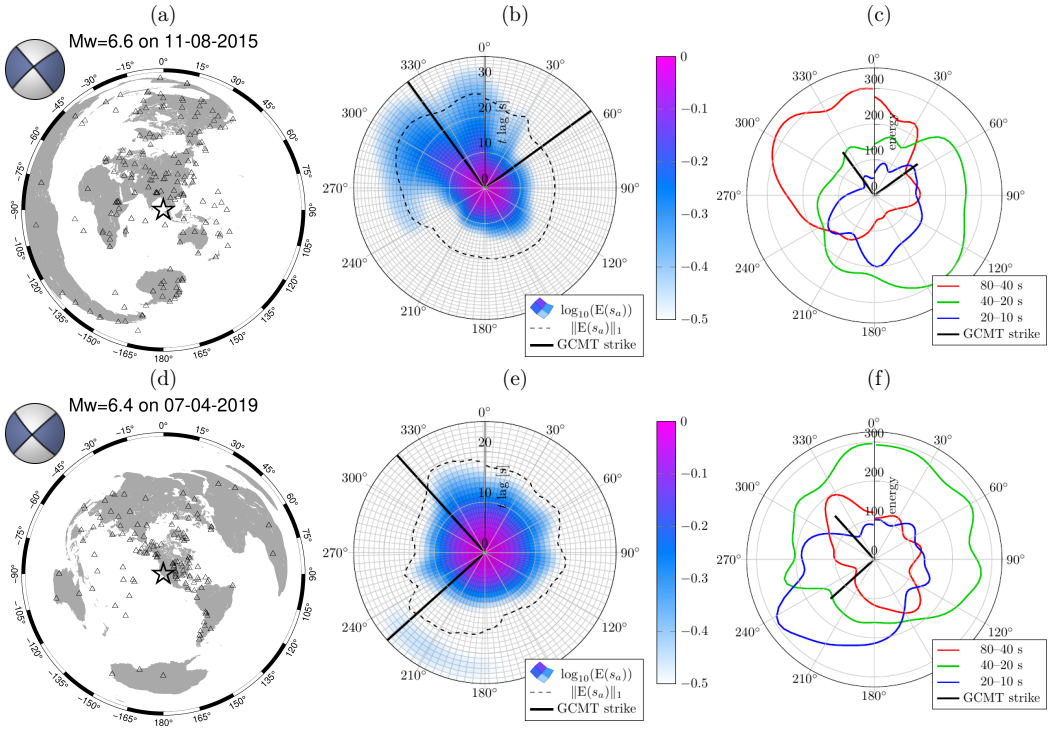


**Figure 3.** FBD of two recorded strike-slip earthquakes. Left column: event (star) and station (triangles) locations. GEOFON moment tensor solutions are inserted. Middle column: the envelope of the estimated auto-correlated apparent source pulse, $E(\hat{s}_{\mathrm{a}}(t;\theta))$ is plotted along with the two possible strike directions (solid radial lines) — note the variation of the source time duration with azimuth. Right column: the source spectral energy vs azimuth plot in three different frequency bands indicates redshift.

trend (USGS, 2019a). Again, note that the rupture propagation is along one of the two possible strike directions, as indicated by the moment tensor in Fig. 3d.

## 5 Conclusions

We have demonstrated that focused blind deconvolution (FBD) is a powerful data-driven tool for factorizing teleseismic records into source and path effects. Instead of relying on source- or path-related assumptions e.g., the empirical Green's function, FBD characterizes an earthquake source by associating it with the similarity among a multitude of records. However, there is a potential problem with this method: it may not succeed due to a number of simplifications (like binning and the Fraunhofer approximation) that were made to arrive at the convolutional model, and there is no theoretical guarantee that FBD performs a physically meaningful factorization even for the convolutional model.

In our numerical experiments, FBD extracted the earthquake source spectra from the surface waves of intermediate-magnitude, shallow strike-slip earthquakes. These spectra are complementary to the ones extracted from other methods using isolated P-wave arrivals. They were further analyzed to identify unilaterally propagating ruptures during the earthquakes; a potential extension is to robustly estimate the rupture velocity. The FBD results of one of the recent recorded earthquakes that originated in

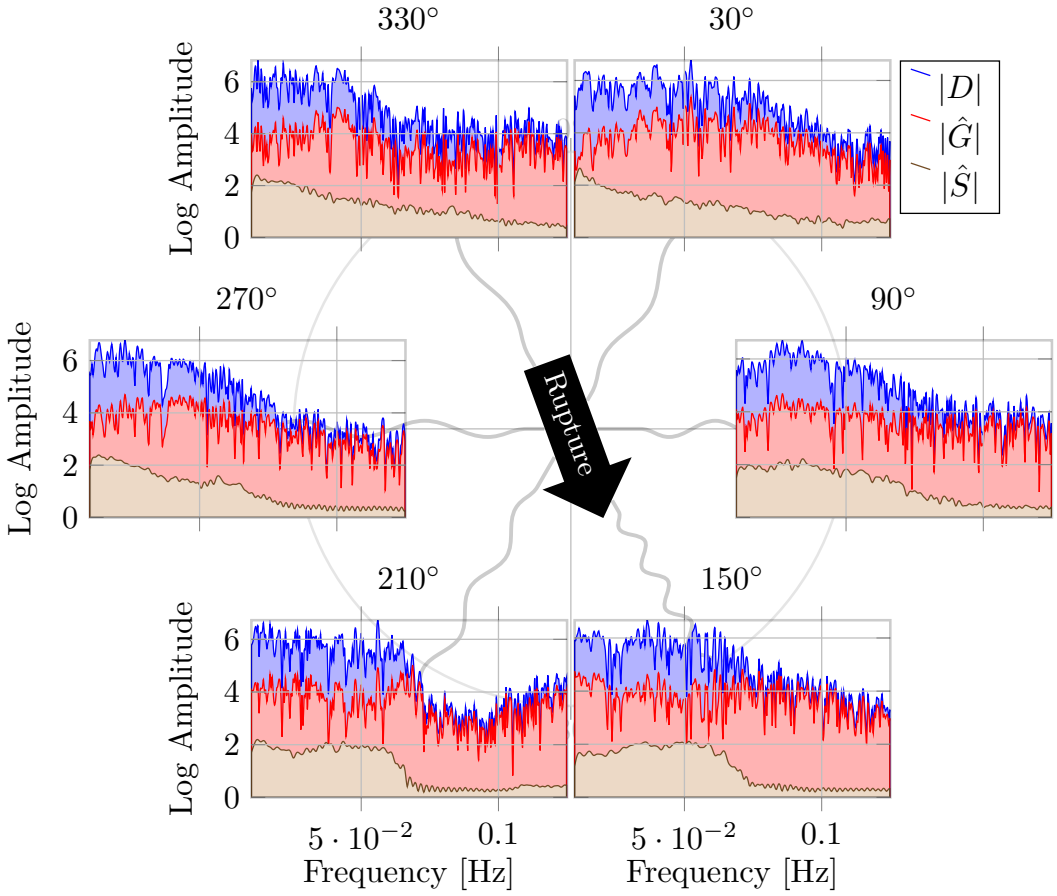


**Figure 4.** FBD factorizes the recorded spectra $|D|$, due to the Nicobar earthquake, into the source $|\hat{S}|$ and the path $|\hat{G}|$ at multiple azimuths. Note that the source spectrum exhibits frequency scaling, with higher corner frequency in the direction of the rupture propagation (indicated by an arrow) and vice versa.

Ridgecrest, California, are consistent with observations from local seismological and geodetic instrumentation — this showcases the potential of FBD to analyze earthquakes without the need of local instrumentation.

## Appendix A Fraunhofer's Approximation

An active fault surface causing an earthquake can be regarded as a surface distribution of body forces (Aki & Richards, 2002). The kinematic dislocation model (Madariaga, 2015) assumes that these equivalent body forces are *activated* in a sequence, depending on the parameter(s) that determine the propagation of the slip. We consider a unidirectional rupture propagation along the length $L$ of a fault plane $\Xi$. The fault plane is assumed to be a rectangle that has a small width $H \ll L$. We denote an infinitesimal surface element at $\xi = (\xi_1, \xi_2)$ on the fault by $d\Xi$, where $\xi_1$ and $\xi_2$ are local two-dimensional coordinates in the length- and width-directions, respectively. In three dimensions, the $i$th component of the far-field displacement at $(\mathbf{x}, t)$ due to a displacement discontinuity across a surface element at $\xi$ can be approximated as:

$$u^i(\mathbf{x}, t; \xi) \approx \sum_{j,k=1}^{3} \int \mathcal{G}^{ij,k}(\mathbf{x}, t-\tau; \xi)\, m^{jk}(\tau; \xi)\, \mathrm{d}\tau, \tag{A1}$$

where $m^{jk}$ denotes the $(j,k)$th component of the moment density tensor and $\mathcal{G}^{ij,k}$ denotes the $k$th spatial derivative of the $(i,j)$th component of the elastodynamic Green's tensor. We now assume an instantaneous slip such that the dependency of the moment density tensor on the time $\tau$ can be ignored. We also assume that the components of the moment density tensor do not vary relative to each other resulting in $m^{jk}(\xi) = h(\xi) m^{jk}(\xi_0)$, where $h(\xi)$ is proportional to the stress drop at $\xi$ and $\xi_0 = (0,0)$ is the hypocenter. Rewriting eq. A1 with these assumptions results in:

$$u^i(\mathbf{x}, t; \xi) \approx h(\xi) g^i(\mathbf{x}, t; \xi), \quad \text{where} \quad g^i(\mathbf{x}, t; \xi) = \sum_{j,k} \mathcal{G}^{ij,k}(\mathbf{x}, t; \xi)\, m^{jk}(\xi_0).$$

In this paper, we refer to the terms 'Green's function' and 'path effects' with $g^i$ of the above equation, even though it already includes some directivity effects e.g., due to a force couple. Also, note that we have dropped the component $i$ (not to be confused with receiver-label $i$) because FBD handles all the measured displacement components identically. Now, consider a constant velocity $c_\mathrm{r}$ for the rupture that propagates or spreads starting from $\xi_1 = 0$ to $\xi_1 = L$. In other words, the slip at the surface element $\xi$ is *activated* with a delay given by $\tau(\xi) = \xi_1 / c_\mathrm{r}$. The total far-field displacement $d$ due to the entire rupture is the sum of contributions from different surface elements:

$$d(\mathbf{x}, t; \Xi) = \int_\Xi h(\xi)\, g(\mathbf{x}, t - \tau(\xi); \xi)\, d\Xi,$$

the contributions being respectively delayed according to $\tau(\xi)$. We now assume that the dominant seismic wavelength $\lambda$ that is under consideration significantly exceeds the width $H$ of the fault, such that $g(\mathbf{x}, t; \xi)$ will be in phase $\forall\, \xi_2$. Accordingly, we can rewrite the above equation using another scalar function $w$ as:

$$d(\mathbf{x}, t) = \int_0^L w(\xi_1)\, g\left(\mathbf{x}, t - \frac{\xi_1}{c_\mathrm{r}}; \xi_1\right) d\xi_1. \tag{A2}$$

In order to limit the dependency of $g$ on the length coordinate $\xi_1$ to an overall translation in time in eq. A2, we make the so-called Fraunhofer approximation, which only makes an allowance for the far-field phase correction (travel-time difference) between 0 and $\xi_1$. For the part of the wavefield associated with waves having velocity $c$

in the source region, we have

$$g(\mathbf{x}, t; \xi_1) \approx g\left(\mathbf{x}, t - \frac{\xi_1 \cos\psi}{c}; 0\right), \tag{A3}$$

where $\psi$ is the direction, relative to the rupture propagation, in which the waves depart from $\Xi$. Aki and Richards (2002) showed that this is a valid first-order approximation in a region, where the receivers are located at large distances

$$|\mathbf{x} - \xi_0| \gg \frac{2L^2}{\lambda}. \tag{A4}$$

Now, combining eqs. A2 and A3 and dropping the redundant argument 0 of $g$, we get:

$$d(\mathbf{x}, t) \quad = \quad \int_0^L w(\xi_1)\, g\left(\mathbf{x}, t - \frac{\xi_1 \gamma}{c_\mathrm{r}}\right) d\xi_1, \quad \text{where} \quad \gamma = 1 - \frac{c_\mathrm{r} \cos\psi}{c} \tag{A5}$$

could be positive, negative or zero. For $\gamma \neq 0$, we now substitute $k = \xi_1 \gamma / c_\mathrm{r}$ that belongs to a time interval $\mathbb{T} = \{t \in \mathbb{R} \mid 0 < t c_\mathrm{r}/\gamma < L\}$ of length $|\gamma| L / c_\mathrm{r}$, to obtain

$$d(\mathbf{x}, t) = \int_{-\infty}^{\infty} s(k; \psi)\, g\left(\mathbf{x}, t - k\right)\, dk, \tag{A6}$$

where the rupture manifests itself in the recorded time as a function commonly known as the apparent source time function (ASTF):

$$\begin{aligned} s(t; \psi) \quad &= \quad \begin{cases} \frac{c_\mathrm{r}}{|\gamma|} w\left(\frac{t c_\mathrm{r}}{\gamma}\right) & \text{when} \quad \gamma \neq 0 \,\&\, t \in \mathbb{T}, \\ 0 & \text{otherwise} \end{cases} \\ &\xrightarrow[\gamma \to 0]{} \quad \delta(t) \int_0^L w(x)\, dx \end{aligned}$$

(a corollary of e.g., Stein & Weiss, 2016, Theorem 1.18). Finally, we time-discretize and rewrite eq. A6 as a temporal convolution

$$u *_t v = \sum_{k=-\infty}^{\infty} u(k)\, v\left(t - k\right) \tag{A7}$$

between the ASTF and the Green's function $g$ to obtain eq. 1

## Appendix B Illustration of FBD Using Random Signals

Focused Blind Deconvolution (FBD) simultaneously maximizing the whiteness of any $g_i$ promotes its dissimilarity from all the $g_{j \neq i}$. To illustrate this, we consider a numerical experiment with $n = 20$ and plot (only for $i = 1, 2, 3$) the spectra associated with two possible solutions of Interferometric Blind Deconvolution (eq. 4) in Figs. Appendix Ba and Appendix Bb, respectively. It can be noted that in both cases the observed spectra are satisfied i.e., $|D_i| = |\hat{S}||\hat{G}_i| \; \forall\, i$. The focusing constraint $J$ is designed to choose the (b) solution because the spectra associated with $g_i$ are maximally white. Also, note that this maximally-white solution has maximum dissimilarity among the $g_i$ spectra; as a result, FBD seeks a solution of the ill-posed IBD where the $g_i$ are dissimilar to each other.

## Appendix C Additional Details of the Earthquakes

The locations and moment-tensor solutions of earthquakes presented in the paper are plotted in the Fig. C1, and also listed in Table C1.

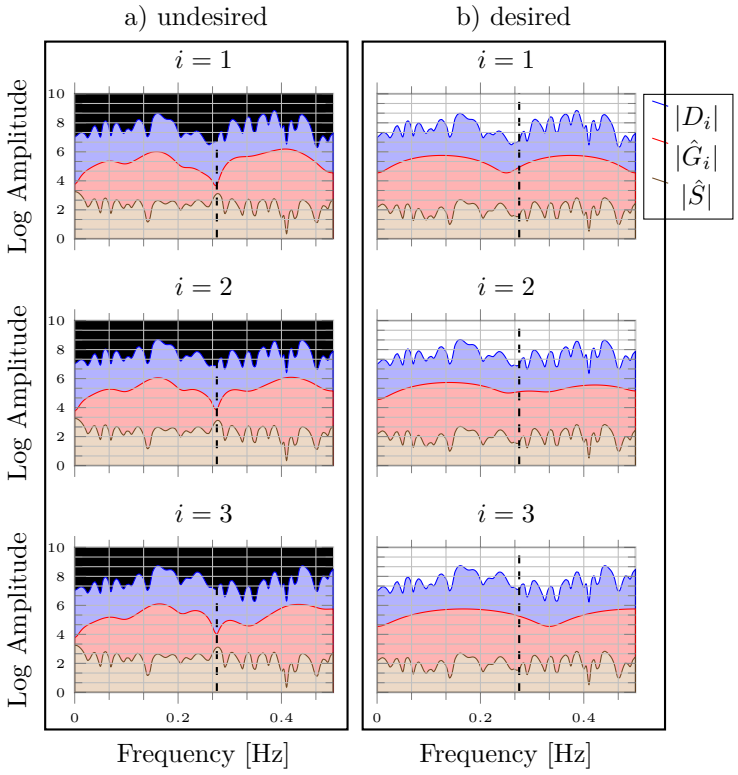


**Figure B1.** Two possible factorizations of the recorded spectra $|D_i|$, associated with the solutions of the IBD problem in eq. 4, are plotted in (a) and (b). Note that in each of the plots the recorded spectrum is satisfied i.e., $\log|D_i| = \log|\hat{G}_i| + \log|\hat{S}|$ as implied by eq. 3. In factorization (a), the estimated spectra associated with the path effects $|\hat{G}_i|$ are *similar* to each other e.g., they have a common notch at the frequency indicated by the dashed line. Therefore, factorization (a) is undesirable, provided that the receivers are separated by distances much larger than the wavelength. The focusing constraint in FBD obtains the factorization (b) —note that the $|\hat{G}_i|$ in this factorization are not only more *white* but also *dissimilar* to each other. Therefore, in the framework of FBD, the *similarities* in the recorded spectra are identified as source $\hat{S}$ effects.

**Table C1.** List of earthquakes along with two possible moment-tensor solutions. Courtesy: GEOFON Earthquake Information Service.

| Name, Date, Mw | Latitude | Longitude | Depth | Strike (°) | Dip (°) | Rake (°) |
|---|---|---|---|---|---|---|
| Nicobar, 2015-11-08, 6.5 | 6.79°N | 94.50°E | 15 km | 321, 230 | 87, 82 | 171, -2 |
| California, 2019-07-04, 6.4 | 35.69°N | 117.46°W | 14 km | 137, 227 | 82, 87 | 177, 8 |

(a) Nicobar Islands, India

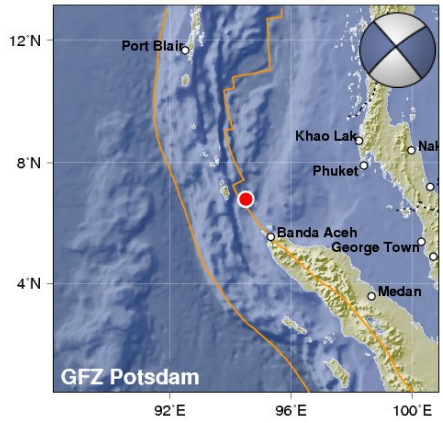


(b) California, USA

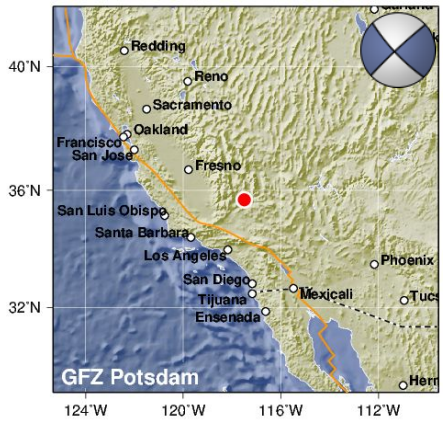


**Figure C1.** Two strike-slip earthquakes that are analyzed in this paper. Major faults in the region are delineated by orange curves, and moment tensor solutions are inserted. Courtesy: GEOFON Program (Hanka & Kind, 1994), GFZ Potsdam.

**Table D1.** List of complex earthquakes with two possible moment-tensor solutions. Courtesy: GEOFON Earthquake Information Service.

| Name, Date, Mw | Latitude | Longitude | Depth | Strike (°) | Dip (°) | Rake (°) |
|---|---|---|---|---|---|---|
| California, 2019-07-05, 7.1 | 35.76°N | 117.57°W | 14 km | 140, 233 | 76, 78 | 167, 14 |
| Loyalty, 2017-10-31, 6.7 | 21.64°S | 169.21°E | 11 km | 154, 321 | 76, 14 | 93, 77 |

## Appendix D More Complex Earthquakes

We analyzed a wide variety of earthquakes in our research, other than those discussed in this article. Most of them were complex, in the sense that it was difficult to interpret the extracted source spectrum directly via redshift attribute. Therefore, additional spectral attributes have to be defined when continuing this research. Here, we present the source spectra of two slightly complex events, listed in Table D1. The locations of these events and their corresponding stations are plotted in Figs. D1a and D1d, respectively.

We first present the FBD analysis for the July 5 mainshock (USGS, 2019b) in the Ridgecrest sequence. Compared to its foreshock, presented in the main text, the estimated auto-correlated source pulse $\hat{s}_a$ in Fig. D1b is complex. However, there is a minor indication that a dominant rupture mode is propagating towards the NW direction — note the longer source-pulse duration around 160° azimuth. Nevertheless, its corresponding spectral-energy vs azimuth plot in Fig. D1c was too complicated to interpret a unilateral propagation.

Similarly, the FBD analysis of a Mw = 6.7 earthquake to the Southeast of Loyalty Islands is presented in Figs. D1d, D1e and D1f. The apparent source-time function estimated using the SCARDEC method (Vallée & Douet, 2016) indicated a duration of silence of about 5 s during the earthquake. This is consistent with the FBD result in Fig. D1e, where $\hat{s}_a$ exhibits a silence during the rupturing for about the same duration. As a result, we conclude that the earthquake didn't consist of a single rupture propagation with a constant velocity.

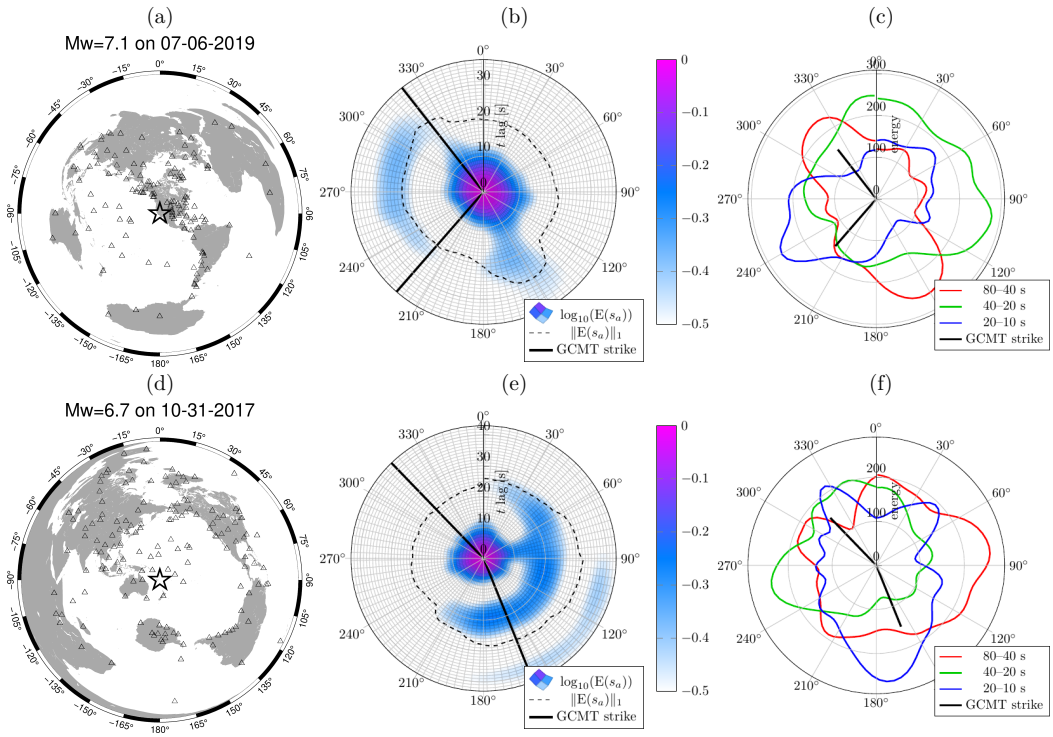


**Figure D1.** As in Fig. 3, except that the FBD results indicate complex rupturing. Redshift due to a unilateral rupture propagation cannot be identified during the analysis of these earthquakes, which are listed in the Table D1.

## Appendix E Software: FocusedBlindDecon.jl

We have made a documented software available to perform focused blind deconvolution through a Julia package: `https://github.com/pawbz/FocusedBlindDecon.jl`.


## Acknowledgments

We thank our colleagues Nafi Toksöz, Matt Li, Aurelien Mordret, Tom Herring, Hongjian Fang and Michael Floyd for providing insight and expertise that greatly assisted this research. The material is based upon work assisted by a grant from Equinor. Any opinions, findings, and conclusions or recommendations expressed in this material are those of the authors and do not necessarily reflect the views of Equinor. LD is also supported by AFOSR grant FA9550-17-1-0316. Finally, we are grateful to the organizations who provide and manage data: Global Seismographic Network (GSN) is a cooperative scientific facility operated jointly by the Incorporated Research Institutions for Seismology (IRIS), the United States Geological Survey (USGS), and the National Science Foundation (NSF), under Cooperative Agreement EAR-1261681. Earthquake information was obtained from the GEOFON programme of the GFZ German Research Centre for Geosciences using data from the GEVN partner networks.


## References


Aki, K., & Richards, P. G. (2002). *Quantitative seismology.*

Ayers, G., & Dainty, J. C. (1988). Iterative blind deconvolution method and its ap-

plications. *Optics letters*, *13*(7), 547-549.
Beyreuther, M., Barsch, R., Krischer, L., Megies, T., Behr, Y., & Wassermann, J. (2010, May). ObsPy: A Python Toolbox for Seismology. *Seismological Research Letters*, *81*(3), 530-533. doi: 10.1785/gssrl.81.3.530
Bharadwaj, P., Demanet, L., & Fournier, A. (2019, June). Focused Blind Deconvolution. *IEEE Transactions on Signal Processing*, *67*(12), 3168-3180. doi: 10.1109/TSP.2019.2908911
Clayton, R. W., & Wiggins, R. A. (1976, October). Source shape estimation and deconvolution of teleseismic bodywaves. *Geophysical Journal International*, *47*(1), 151-177. doi: 10.1111/j.1365-246X.1976.tb01267.x
Dziewonski, A. M., Chou, T.-A., & Woodhouse, J. H. (1981). Determination of earthquake source parameters from waveform data for studies of global and regional seismicity. *Journal of Geophysical Research: Solid Earth*, *86*(B4), 2825-2852. doi: 10.1029/JB086iB04p02825
Gallovic, F., Valentova, L., Ampuero, J.-P., & Gabriel, A.-A. (2019, February). *Bayesian Dynamic Finite-Fault Inversion: 1. Method and Synthetic Test* (Preprint). EarthArXiv. doi: 10.31223/osf.io/tmjv4
Hanka, W., & Kind, R. (1994, November). The GEOFON Program. *Annals of Geophysics*, *37*(5). doi: 10.4401/ag-4196
Hartzell, S. H. (1978, January). Earthquake aftershocks as Green's functions. *Geophysical Research Letters*, *5*(1), 1-4. doi: 10.1029/GL005i001p00001
Heaton, T. H., & Helmberger, D. V. (1977, April). A study of the strong ground motion of the Borrego Mountain, California, earthquake. *Bulletin of the Seismological Society of America*, *67*(2), 315-330.
Hosseini, K., & Sigloch, K. (2017, October). ObspyDMT: A Python toolbox for retrieving and processing large seismological data sets. *Solid Earth*, *8*(5), 1047-1070. doi: 10.5194/se-8-1047-2017
Kikuchi, M., & Kanamori, H. (1982). Inversion of complex body waves. *Bulletin of the Seismological Society of America*, *72*(2), 491-506.
Lanza, V., Spallarossa, D., Cattaneo, M., Bindi, D., & Augliera, P. (1999, June). Source parameters of small events using constrained deconvolution with empirical Green's functions. *Geophysical Journal International*, *137*(3), 651-662. doi: 10.1046/j.1365-246x.1999.00809.x
Larmat, C., Montagner, J.-P., Fink, M., Capdeville, Y., Tourin, A., & Clévédé, E. (2006). Time-reversal imaging of seismic sources and application to the great Sumatra earthquake. *Geophysical Research Letters*, *33*(19). doi: 10.1029/2006GL026336
Lay, T., Kanamori, H., Ammon, C. J., Hutko, A. R., Furlong, K., & Rivera, L. (2009, November). The 2006-2007 Kuril Islands great earthquake sequence: THE 2006-2007 KURIL ISLANDS EARTHQUAKES. *Journal of Geophysical Research: Solid Earth*, *114*(B11). doi: 10.1029/2008JB006280
Madariaga, R. (2015). Seismic Source Theory. In *Treatise on Geophysics* (p. 51-71). Elsevier. doi: 10.1016/B978-0-444-53802-4.00070-1
McGuire, J. J. (2004, April). Estimating Finite Source Properties of Small Earthquake Ruptures. *Bulletin of the Seismological Society of America*, *94*(2), 377-393. doi: 10.1785/0120030091
Meng, C., & Wang, H. (2018, April). A finite element and finite difference mixed approach for modeling fault rupture and ground motion. *Computers & Geosciences*, *113*, 54-69. doi: 10.1016/j.cageo.2018.01.015
Meng, L., Zhang, A., & Yagi, Y. (2016). Improving back projection imaging with a novel physics-based aftershock calibration approach: A case study of the 2015 Gorkha earthquake. *Geophysical Research Letters*, *43*(2), 628-636. doi: 10.1002/2015GL067034
Olson, A. H., & Apsel, R. J. (1982, December). Finite faults and inverse theory with applications to the 1979 Imperial Valley earthquake. *Bulletin of the Seismolog-*

*ical Society of America*, *72*(6A), 1969-2001.

Plourde, A. P., & Bostock, M. G. (2017, June). Multichannel Deconvolution for Earthquake Apparent Source Time Functions. *Bulletin of the Seismological Society of America*, ssabull;0120170015v1. doi: 10.1785/0120170015

Sibul, L., & Ziomek, L. (1981, March). Generalized wideband crossambiguity function. In *ICASSP '81. IEEE International Conference on Acoustics, Speech, and Signal Processing* (Vol. 6, p. 1239-1242). doi: 10.1109/ICASSP.1981.1171180

Somala, S. N., Ampuero, J.-P., & Lapusta, N. (2018, July). Finite-fault source inversion using adjoint methods in 3-D heterogeneous media. *Geophysical Journal International*, *214*(1), 402-420. doi: 10.1093/gji/ggy148

Sroubek, F., & Milanfar, P. (2012). Robust multichannel blind deconvolution via fast alternating minimization. *IEEE Transactions on Image Processing*, *21*(4), 1687-1700.

Stein, E. M., & Weiss, G. (2016). *Introduction to Fourier Analysis on Euclidean Spaces (PMS-32)*. Princeton University Press.

Tocheport, A., Rivera, L., & Chevrot, S. (2007). A systematic study of source time functions and moment tensors of intermediate and deep earthquakes. *Journal of Geophysical Research: Solid Earth*, *112*(B7).

Ulrych, T. J. (1971, August). Application of homomorphic deconvolution to seismology. *GEOPHYSICS*, *36*(4), 650-660. doi: 10.1190/1.1440202

USGS. (2019a, July). *Ridgecrest M 6.4; 11km SW of Searles Valley, CA.* https://earthquake.usgs.gov/earthquakes/eventpage/ci38443183/executive.

USGS. (2019b, May). *Ridgecrest M 7.1; 11km SW of Searles Valley, CA.* https://earthquake.usgs.gov/earthquakes/eventpage/ci38457511/executive.

Vallée, M., Charléty, J., Ferreira, A. M., Delouis, B., & Vergoz, J. (2011). SCARDEC: A new technique for the rapid determination of seismic moment magnitude, focal mechanism and source time functions for large earthquakes using body-wave deconvolution. *Geophysical Journal International*, *184*(1), 338-358.

Vallée, M., & Douet, V. (2016). A new database of source time functions (STFs) extracted from the SCARDEC method. *Physics of the Earth and Planetary Interiors*, *257*, 149-157.

Weiss, L. G. (1994, January). Wavelets and wideband correlation processing. *IEEE Signal Processing Magazine*, *11*(1), 13-32. doi: 10.1109/79.252866

Yin, J., & Denolle, M. A. (2019, May). Relating teleseismic backprojection images to earthquake kinematics. *Geophysical Journal International*, *217*(2), 729-747. doi: 10.1093/gji/ggz048